Prediction of the Clinical SUV Ratio in Amyloid PET Imaging Using a Biomathematic Modeling Approach Toward the Efficient Development of a Radioligand

Yuma Arakawa*[1], YingHwey Nai*[2], Miho Shidahara[1,3], Shozo Furumoto[4], Chie Seki[5], Nobuyuki Okamura[6], Manabu Tashiro[2], Yukitsuka Kudo[7], Kazuhiko Yanai[6], Kohsuke Gonda[1], and Hiroshi Watabe[3]

[1]Department of Medical Physics, Tohoku University Graduate School of Medicine, Sendai, Japan; [2]Division of Radiation Protection and Safety Control, Cyclotron and Radioisotope Center, Tohoku University, Sendai, Japan; [3]Division of Cyclotron Nuclear Medicine, Cyclotron and Radioisotope Center, Tohoku University, Sendai, Japan; [4]Division of Radiopharmaceutical Chemistry, Cyclotron and Radioisotope Center, Tohoku University, Sendai, Japan; [5]Biophysics Program, Molecular Imaging Center, National Institute of Radiological Sciences, Chiba, Japan; [6]Department of Pharmacology, Tohoku University School of Medicine, Sendai, Japan; and [7]Division of Neuro-Imaging, Institute of Development, Ageing and Cancer, Tohoku University, Sendai, Japan

Our study aimed to develop a method to mathematically predict the kinetic parameters K_1 (influx rate constant), k_2 (efflux rate constant), and BP_{ND} (nondisplaceable binding potential) of amyloid PET tracers and obtain SUV ratios (SUVRs) from predicted time–activity curves of target and reference regions. **Methods:** We investigated 10 clinically applied amyloid PET radioligands: ^{11}C-Pittsburgh compound B, ^{11}C-BF-227, ^{11}C-AZD2184, ^{11}C-SB-13, ^{18}F-FACT, ^{18}F-florbetapir, ^{18}F-florbetaben, ^{18}F-flutemetamol, ^{18}F-FDDNP, and ^{18}F-AZD4694. For each tracer, time–activity curves of both target and reference regions were generated using a simplified 1-tissue-compartment model, with an arterial plasma input function and the predicted kinetic parameters. K_1, k_2, and BP_{ND} were derived from the lipophilicity (log$P$), apparent volume, free fraction in plasma, free fraction in tissue, dissociation constant, and density of amyloid β using biomathematic modeling. Density was fixed at 3 nM to represent healthy control conditions and 50 nM to represent severe Alzheimer disease (AD). Predicted SUVRs for the healthy and AD groups were then obtained by dividing the integrated time–activity curve of the target region by that of the reference region. To validate the presented method, the predicted K_1, k_2, BP_{ND}, and SUVR for the healthy and AD groups were compared with the respective clinically observed values. **Results:** The correlation between predicted and clinical kinetic parameters had an R^2 value of 0.73 for K_1 in the healthy group, 0.71 for K_1 in the AD group, 0.81 for k_2 in the healthy group, 0.85 for k_2 in the AD group, and 0.63 for BP_{ND} in the AD group. The regression relationship between the predicted SUVR (y) and the clinical SUVR (x) for the healthy and the AD groups was $y = 2.73x - 2.11$ ($R^2 = 0.72$). **Conclusion:** The proposed method showed a good correlation between predicted and clinical SUVR for the 10 clinically applied amyloid tracers.

Aggregation of amyloid β (Aβ) peptide is one of the pathologic observations in the brains of individuals with Alzheimer disease (AD). Amyloid imaging using PET allows quantitative visualization of Aβ deposition in the living human brain (*1*). In the last decade, many PET radioligands have been developed for amyloid imaging. Some of these have successfully been applied in human PET studies: for example, ^{11}C-Pittsburgh compound B (PIB) (*2*), ^{11}C-labeled 2-(2-[2-dimethylaminothiazol-5-yl]ethenyl)-6-(2-[fluoro]ethoxy)benzoxazole (^{11}C-BF-227) (*3–6*), ^{11}C-labeled 5-(6-{[tert-butyl(dimethyl)silyl]oxy}-1,3-benzothiazol-2-yl)pyridin-2-amine (^{11}C-AZD2184) (*7*), ^{11}C-4-*N*-methylamino-4′-hydroxystilbene (^{11}C-SB-13) (*8*), ^{18}F-2-[2-{(E)-2-[2-(dimethylamino)-1,3-thiazol-5-yl]vinyl}-1,3-benzoxazol-6-yl)oxy]-3-fluoropropan-1-ol (^{18}F-FACT) (*4*), ^{18}F-florbetapir (Amyvid; Eli Lilly and Company) (*9,10*), ^{18}F-florbetaben (Neuraceq; Piramal Imaging) (*11*), ^{18}F-flutemetamol (Vizamyl; GE Healthcare) (*12,13*), 2-(1-{6-[(2-^{18}F-fluoroethyl)(methyl)amino]-2-naphthyl}ethylidene)malonitrile (^{18}F-FDDNP) (*14*), and 2-[2-^{18}F-fluoro-6-(methylamino)-3-pyridinyl]-1-benzofuran-5-ol (^{18}F-AZD4694) (*15*).

In general, the discovery and development of radioligands for clinical application requires complicated and sometimes empiric procedures in terms of chemical factors (e.g., stability of labeling and lipophilicity) or biologic factors (e.g., affinity, metabolites, and density [B_{avail}] of the target) (*16,17*). The radioligand should preferably bind with high affinity to target molecules while having a low affinity for other nonspecific binding sites (*18*). It is also expected that the radioligand will readily cross the blood–brain barrier and bind with the target whereas its undesirable metabolites will not penetrate the blood–brain barrier. Lipophilicity is often expressed as the logarithm of the partition coefficient (log$P$) or distribution coefficient (log$D$), and its optimal range for central nervous system (CNS) drugs with high permeability has been reported to vary from 1 to 3 (*19*). The dissociation constant

(K_D) is the index for affinity and is measured through in vitro binding experiments. Even though these factors have been well investigated in the case of candidate radioligands, several factors obtained through in vitro or in vivo animal studies may not be applicable to human studies, and it is not easy to develop successful radioligands and satisfy clinical demands (20). We need to know not only the microparameters of the candidate radioligands but also their overall macroscopic performance.

Recently, there has been growing interest in more efficient development of successful radioligands in clinical studies using systematic evaluation of their overall performance (e.g., outcome measures). It is obvious that the use of in vivo PET scans in animals or humans is the fastest and easiest approach to evaluating the overall performance of the candidate radioligand. However, the development of a labeling protocol for positron emitter isotopes, and the synthesis of a radioligand for PET studies, are labor-intensive and lengthy processes. A systematic screening method for CNS radioligands without the use of in vivo PET scans was proposed by Guo et al. (17). Their method mathematically simulates clinical dynamic PET data for each candidate radioligand using the kinetic parameters K_1 (influx rate constant) and k_2 (efflux rate constant) between arterial plasma and brain tissue and the kinetic parameter BP_{ND} (nondisplaceable binding potential) (16) with fluctuations in statistical noise and the human population (21). The kinetic parameters were derived from biomathematic modeling using the logarithm of the distribution coefficient, taking into account several variables: all the neutral and charged forms of the molecule ($clogD$); the apparent molecular volume, or McGowan volume (cm^3/mol/100) (V_x); the free fraction of radioligand in plasma (f_p); the free fraction of nondisplaceable radioligand in brain tissue (f_{ND}); and the K_D and B_{avail} of the target molecules. Good radioligands were screened out by comparing coefficients of variation for the estimated BP_{ND} (17). However, the approach includes in vitro animal experiments and analysis using liquid chromatography–tandem mass spectrometry for f_P and f_{ND}, and it is difficult to achieve

high reproducibility and reliability among different researchers and facilities. The approach has been applied only for CNS radioligands, not for amyloid PET tracers.

We proposed a new method to predict the SUV ratio (SUVR) of amyloid PET radioligands using biomathematic modeling and an in silico parameter; here, we use the words *in silico* to indicate numerically computed. SUVR is a common outcome measure in clinical amyloid PET imaging because it does not require use of arterial blood sampling and long dynamic PET scans. Furthermore, instead of using in vitro measurement of f_p and f_{ND}, we investigated a surrogate method of measurement using a regression relationship determined from previously reported datasets of in silico $logP$, in vitro f_{ND}, and f_P. The applicability and reliability of the proposed method in predicting the SUVRs of amyloid radioligands were validated using previously clinically observed kinetic parameters and the SUVRs for ^{11}C-PIB, ^{11}C-BF-227, ^{11}C-AZD2184, ^{11}C-SB-13, ^{18}F-FACT, ^{18}F-florbetapir, ^{18}F-florbetaben, ^{18}F-flutemetamol, ^{18}F-FDDNP, and ^{18}F-AZD4694.

MATERIALS AND METHODS

Amyloid PET Radioligands

Ten clinically applied amyloid radioligands (^{11}C-PIB, ^{11}C-BF-227, ^{11}C-AZD2184, ^{11}C-SB-13, ^{18}F-FACT, ^{18}F-florbetapir, ^{18}F-florbetaben, ^{18}F-flutemetamol, ^{18}F-FDDNP, and ^{18}F-AZD4694) were evaluated in this study. The measured K_D for these ligands and the clinical SUVRs are detailed in Table 1. We selected the clinical SUVRs for specific cortical regions that show the highest SUVR in AD patients. The chemical structures of all radioligands, excepting ^{18}F-FACT, were downloaded from PubChem (https://pubchem.ncbi.nlm.nih.gov) and used in the prediction study. The chemical structure of ^{18}F-FACT was manually drawn using commercial software.

Biomathematic Modeling

We assumed that the radioligand of interest obeyed the simplified 1-tissue-compartment model (Fig. 1A). The kinetic parameters in the

TABLE 1
Binding Properties of 10 Amyloid PET Radioligands

	K_D (nM)			Clinical SUVR (−)				
Radioligand	Aβ$_{1-40}$	Aβ$_{1-42}$	Ref.	Interval (min)	Region	Healthy	AD	Ref.
[11]C-PIB	1.02, 0.90, 3.30, 4.70, (2.48)*	0.91, 0.95, (0.93)*	1,37–39	40–60	Posterior cingulate	1.32	2.79	2
[11]C-BF-227	1.8	4.3	5	40–60	Temporal occipital	1.32	1.65	4
[11]C-AZD2184	8.40	—	38	40–60	Posterior cingulate	1.24	2.54	7
[11]C-SB-13	2.43†		8	40–120	Left frontal	—	1.34	8
^{18}F-FACT	9.40	—	30	40–60	Temporal occipital	1.25	1.33	4
[18]F-florbetapir	3.72†		40	50–60	Precuneus	1.30	1.85	9
[18]F-florbetaben	2.22‡		41	90–120	Gyrus rectus	1.37	2.15	11
[18]F-flutemetamol	1.60	—	42	85–115	Precuneus	1.36	2.16	13
^{18}F-FDDNP	0.12	5.52	32,43	45–55	Anterior cingulate	1.24	1.37	14
^{18}F-AZD4694	2.30	—	42	51–63	Prefrontal	1.15	2.88	36

*Averaged K_D.
†Binding affinity to brain homogenate in AD subject.
‡K_D with florbetapir to brain homogenate in AD subject.
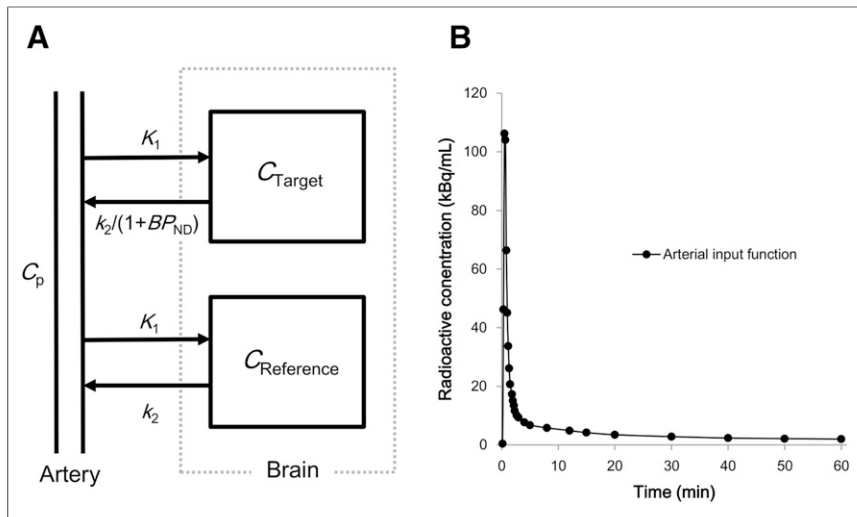Ref. = reference.

FIGURE 1. (A) One-tissue-compartment model for both target and reference regions. (B) Measured human plasma input function $C_p(t)$ for ^{11}C-BF227 used in simulation.

human brain for each radioligand were mathematically modeled. The time–activity curves, with or without specific binding of the radioligand in brain tissue, were calculated as follows:

$$C_{target}(t) = K_1 \cdot C_p(t) \otimes \exp\left[-\left(\frac{k_2}{1 + BP_{ND}}\right)t\right]$$

$$C_{reference}(t) = K_1 \cdot C_p(t) \otimes \exp(-k_2 t). \qquad \text{Eq. 1}$$

In this equation, C_{target} is the time–activity curve of the target region, where the radioligand specifically binds to the target protein; $C_{reference}$ is the time–activity curve of the reference region without the target protein; and C_p is the arterial plasma input function. K_1 from plasma to brain tissue (mL/cm^3/min) was formulated using the Renkin–Crone model as follows:

$$K_1 = f \cdot \left[1 - e^{(-PS/f)}\right], \qquad \text{Eq. 2}$$

where P, f, and S are capillary permeability (cm/min), perfusion (mL/cm^3/min), and capillary surface area (cm^2/cm^3 of brain), respectively. f and S were set to 0.6 and 150, respectively. A scaling factor for K_1, 3.43, was introduced to compensate for the difference between in vivo K_1 and predicted K_1 and was determined by Guo et al. (17) using 13 CNS radioligands that are known to exhibit passive diffusion. Permeability in Equation 2 was empirically formulated as follows (17):

$$P = 10^{\left\{-0.121(clogD - 2.298)^2 - 2.544\log\left(V_x^{1/3}\right) - 2.525\right\}}. \qquad \text{Eq. 3}$$

The k_2 from brain tissue to plasma (1/min) was expressed using the following equation, assuming equilibrium in the radioligand concentrations between plasma and brain tissue:

$$k_2 = \frac{V_{aq\_P} \cdot K_1}{V_{aq\_T}} \cdot \frac{f_{ND}}{f_P}, \qquad \text{Eq. 4}$$

where V_{aq_p} and V_{aq_T} are the apparent aqueous volume in plasma (solvent/mL of plasma) and the apparent aqueous volume in tissue (solvent/mL of tissue), respectively. These were set to 0.98 and

0.9, respectively (17). The radioligand's BP_{ND} at the target site was expressed as follows:

$$BP_{ND} = f_{ND}\frac{B_{avail}}{K_D}, \qquad \text{Eq. 5}$$

where B_{avail} and K_D are in units of nmol/L. The time–activity curves of the target and reference regions were calculated using K_1, k_2, and BP_{ND} and the arterial input function C_p (Fig. 1B) using Equation 1. The parameter of interest, SUVR, was then estimated from the predicted time–activity curves.

Prediction of Clinical SUVR in Amyloid PET Imaging

For each amyloid radioligand, brain permeability in Equation 3 was estimated from V_x and lipophilicity calculated using the commercial software dProperties (Talete SRL). Instead of $clogD$ in Equation 3, we used the in silico Moriguchi log$P$ (22). K_1 was then calculated as detailed in Equation 2.

The k_2 in Equation 4 was estimated from K_1, f_P, and f_{ND}. f_P and f_{ND} were estimated from in vitro binding experiments using mouse brain and plasma and the in silico lipophilicity of 24 CNS drugs (e.g., risperidone, haloperidol, and fluvoxamine) reported by Wan et al. (23) and Maurer et al. (24). The datasets were obtained from references, and then the regression relationships for $clogP$ versus f_{ND} and f_{ND} versus f_P were determined. After a specific radioligand was given, the corresponding f_P and f_{ND} were estimated from these regression lines.

In amyloid PET imaging, B_{avail} in Equation 5 can be regarded as the available binding sites of Aβ fibrils in vivo on aggregate surfaces. The nominal concentration of Aβ fibrils in the frontal, temporal, and parietal cortices of the healthy control and AD subjects was less than 3 nM and 60 nM, respectively, in postmortem human brain tissue (25). Therefore, we regarded the approximate available binding concentrations (B_{avail}) of Aβ fibrils in healthy and severe AD conditions as 3 nM and 50 nM, respectively. Furthermore, there exist several Aβ peptides that are combined with a different number of amino acids. In the human brain, Aβ$_{1-40}$ and Aβ$_{1-42}$ are major binding sites for amyloid radioligands. Therefore, we rearranged Equation 5 as follows:

$$BP_{ND} = f_{ND}\left\{\frac{B_{avail-42}}{K_{D-42}} + \frac{B_{avail-40}}{K_{D-40}}\right\} = f_{ND}\left\{\frac{a}{K_{D-42}} + \frac{(1-a)}{K_{D-40}}\right\}B_{avail}$$

$$B_{avail} = B_{avail-42} + B_{avail-40}, \qquad \text{Eq. 6}$$

where a, K_{D-42}, and K_{D-40} are the fractions of Aβ$_{1-42}$, the K_D for Aβ$_{1-42}$, and the K_D for Aβ$_{1-40}$, respectively. $B_{avail-42}$, $B_{avail-40}$, and B_{avail} are the available binding sites of Aβ$_{1-42}$ and Aβ$_{1-40}$, (Aβ$_{1-42}$ + Aβ$_{1-40}$). a was assumed to have a value of 0.7, which is biochemically derived from fractions of extracellular insoluble Aβ$_{1-42}$ in both AD and healthy brains (26). When neither K_{D-42} nor K_{D-40} was reported (e.g., ^{18}F-FACT in Table 1), BP_{ND} was calculated from the only reported K_D, estimated f_{ND}, and fixed B_{avail} using Equation 5 and not Equation 6.

For amyloid PET radioligands, the outcome measure was set to cortical SUVR with cerebellum as the reference region. For each of the 10 radioligands in subjects with a specific disease status (AD or healthy), SUVR was calculated using the time–activity curves in the
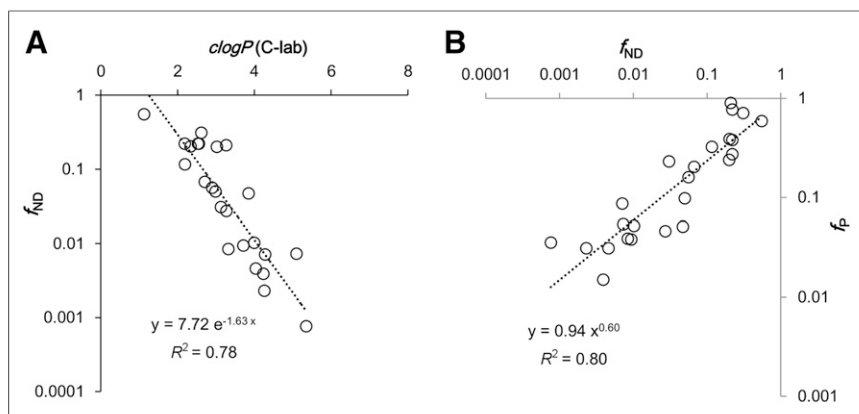
FIGURE 2. Relationship between log$P$ and f_{ND} (A) and between f_{ND} and f_P (B) from previously reported datasets of in silico log$P$ and in vitro f_{ND} and f_P.

target and reference regions predicted from the kinetic parameters as follows:

$$\text{SUVR} = \frac{\int_{t_1}^{t_2} C_{\text{target}}(t)\,dt}{\int_{t_1}^{t_2} C_{\text{reference}}(t)\,dt}, \qquad \text{Eq. 7}$$

where t_1 and t_2 are the start and end of the time interval for SUVR.

Evaluation of the Method

The predicted K_1, k_2, BP$_{ND}$, and SUVR were compared with their clinical counterparts. Clinical K_1 and k_2 for the AD and healthy groups were previously estimated from clinical PET images using the 2-tissue-compartment model with measured arterial plasma input function. With the exception of ^{18}F-FDDNP and ^{18}F-florbetapir, the clinical BP$_{ND}$ was calculated as DVR-1, where DVR is the ratio of the estimated distribution volumes (V_T) using the 2-tissue-compartment model in the target and reference regions (16). For each radioligand, the time intervals for the predicted SUVR in Equation 7 were set to the same values as applied in the clinical study (Table 1). For all simulations, a common input function, shown in Figure 1B, was used. This input function was the averaged plasma input function for ^{11}C-BF227 in 6 healthy subjects and was obtained from Figure 3 in a previous publication (4). The arterial blood was sampled from 0 to 60 min but was linearly extrapolated to 150 min for simulation of ^{11}C-SB-13, ^{18}F-florbetaben, and ^{18}F-flutemetamol.

RESULTS

Regression Relationship of f_P vs. f_{ND} and f_{ND} vs. log$P$

Figure 2A shows the relationships between in silico lipophilicity and in vitro f_{ND}, and Figure 2B shows the relationships between in vitro f_{ND} and f_P using the datasets of Wan et al. (23) and Maurer et al. (24). Good correlations were observed between lipophilicity and f_{ND} and between f_{ND} and f_P (R^2 = 0.78 and 0.80, respectively). As shown in Table 2, f_p and f_{ND} were estimated for each amyloid radioligand using in silico lipophilicity (Moriguchi log$P$) and the regression lines shown in Figure 2.

Predicted K_1, k_2, and BP$_{ND}$

Table 3 shows the predicted and clinical K_1 and k_2 for 8 of the amyloid radioligands. The relationship between predicted and clinical K_1 and between predicted and clinical k_2 is plotted in Figures 3A and 3B, respectively. Because the predicted K_1 and k_2 were derived from the model independently of disease, there is no distinction between the healthy and AD groups in predicted K_1 and k_2, whereas clinical K_1 and k_2 were from the healthy group and the AD group, respectively (Fig. 3A and 3B).

Predicted K_1 correlated positively with clinical K_1 in the healthy group (R^2 = 0.73) and, after exclusion of the outlier (^{18}F-FDDNP), in the AD group as well (R^2 = 0.71). The slope of the regression lines for predicted and clinical K_1 in the AD group (3.02) was larger than that in the healthy group (1.82). The correlation between predicted and clinical k_2 in the healthy and AD groups had an R^2 value of 0.81 and 0.85, respectively. The slope of the regression lines for predicted and clinical k_2 in the AD group (1.53) was larger than that in the healthy group (0.76). Predicted

TABLE 2
In Silico Chemical and Biologic Properties for Prediction of SUVR in 10 Amyloid PET Radioligands

| Radioligand | In silico | | Predicted from datasets | | |
	V_x (cm³/mol/100)	Lipophilicity (Moriguchi log$P$)	f_P	f_{ND}	K_D for simulation
[11]C-PIB	1.88	2.40	0.303	0.152	1.40
[11]C-BF-227	2.33	2.40	0.304	0.153	3.55
[11]C-AZD2184	1.84	1.75	0.573	0.441	8.40
[11]C-SB-13	1.86	3.23	0.135	0.040	2.43
^{18}F-FACT	2.53	1.87	0.511	0.365	9.40
[18]F-florbetapir	2.80	2.52	0.270	0.126	3.72
[18]F-florbetaben	2.84	3.11	0.152	0.048	2.22
[18]F-flutemetamol	1.89	2.80	0.205	0.080	1.60
^{18}F-FDDNP	2.31	2.89	0.187	0.068	3.90
^{18}F-AZD4694	1.79	2.41	0.300	0.150	2.30

TABLE 3
Predicted and Clinically Estimated K_1 and k_2 of 8 Amyloid PET Radioligands in Cortical Region

Radioligand	K_1 (mL/100 g/min)			k_2 (min^{-1})			Regions of interest for clinical study	Ref.
	Predicted K_1	Clinical K_1		Predicted k_2	Clinical k_2			
		Healthy	AD		Healthy	AD		
^{11}C-PIB	0.73	0.29	0.26	0.40	0.17	0.12	Middle precuneus	44
^{11}C-BF-227	0.63	0.27	0.23	0.34	0.13	0.12	Temporal occipital	4
^{11}C-AZD2184	0.69	0.32	0.26	0.58	0.52	0.30	Posterior cingulate	7
^{11}C-SB-13	0.60	—	—	0.19	—	—	—	—
^{18}F-FACT	0.57	0.22	0.20	0.44	0.23	0.16	Temporal occipital	4
^{18}F-florbetapir	0.54	—	—	0.28	—	—	—	—
^{18}F-florbetaben	0.47	0.22	0.19	0.16	0.085	0.076	Frontal cortex	45
^{18}F-flutemetamol	0.69	0.25	0.23	0.29	0.080	0.080	Global cortex*	34
^{18}F-FDDNP	0.58	0.25	0.36	0.23	0.060	0.060	Global cortex†	33
^{18}F-AZD4694	0.75	0.34	0.23	0.41	0.30	0.14	Posterior cingulate	36

*Frontal, parietal, anterior cingulate, posterior cingulate, and temporal cortices.

†Orbital frontal, medial inferior frontal, anterior cingulate, superior temporal, parietal, medial inferior temporal, superior frontal, and entorhinal cortices and hippocampus.

Ref. = reference.

Clinical K_1 and k_2 for healthy and AD groups were estimated using 2-tissue-compartment model with measured arterial input function.

and clinical BP$_{ND}$ for 9 of the amyloid radioligands is detailed in Table 4. Predicted BP$_{ND}$ correlated positively with clinical BP$_{ND}$ in the AD group ($R^2 = 0.63$) (Fig. 3C).

Predicted SUVR

Figure 4 shows the correlation between predicted and clinical SUVR in the healthy and AD groups. Predicted SUVR (y) and clinical SUVR (x) correlated well ($y = 2.73x - 2.11$; $R^2 = 0.72$). Regarding the individual radioligands, ^{11}C-PIB differed from the regression lines slightly.

DISCUSSION

In a move toward finding a more efficient way to screen successful PET radioligands for clinical use, we have proposed a

method of predicting the SUVR of amyloid PET radioligands. Rather than predicting other macroparameters, such as DVR as SUVR, we chose to predict SUVR because it is the most frequently used parameter in clinical studies, as it can be obtained without arterial blood sampling or dynamic PET scans and can be computed using a portion of the time–activity curve.

Predicted Permeability and K_1

Permeability is an important parameter for the prediction of K_1 in Equation 2. Guo et al. (17) estimated permeability according to Equation 3. However, $clogD$ in Equation 3 was computed using in-house software (17) that was not available to us; thus, we used the Moriguchi log$P$ as an alternative. Nonetheless, we found a positive correlation between predicted K_1 and clinical K_1 (Fig. 3A), although predicted K_1 was slightly overestimated. There are
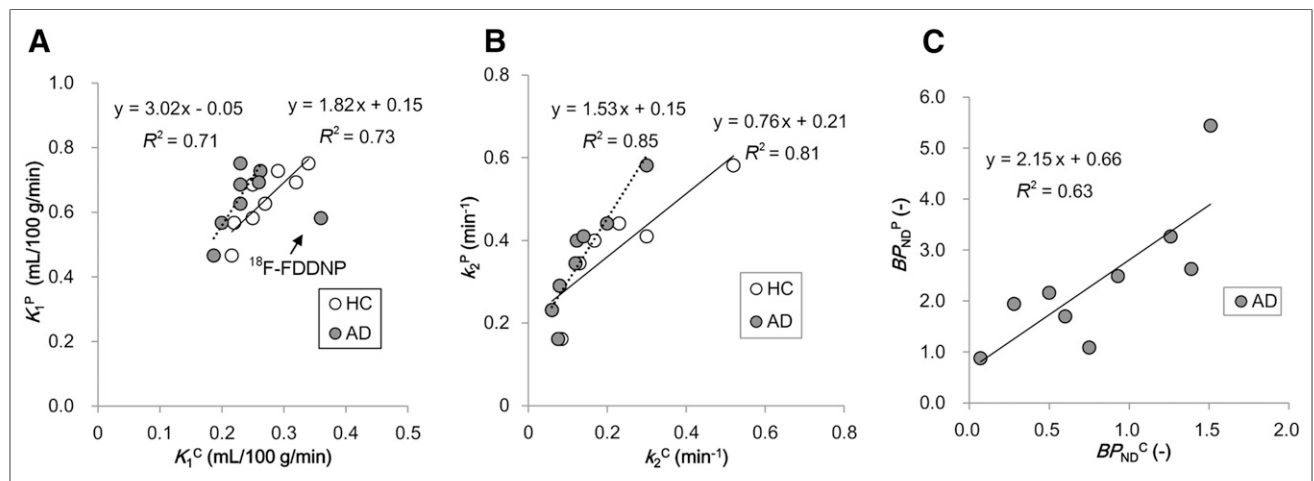

FIGURE 3. Comparison between predicted (y-axis) and clinical (x-axis) K_1 (A), k_2 (B), and BP$_{ND}$ (C) datasets in cortical regions. HC = healthy control.

TABLE 4
TABLE 4
Predicted and Clinical BP$_{ND}$ (−) for 9 Amyloid PET Radioligands

| Radioligand | Predicted BP$_{ND}$ (B_{avail} = 50 nM) | Clinical BP$_{ND}$ | | Ref. |
		AD	ROI	
^{11}C-PIB	5.44	1.51	Posterior cingulate*	2
^{11}C-BF-227	2.16	0.50	Temporal occipital*	4
^{11}C-AZD2184	2.63	1.39	Posterior cingulate*	7
^{11}C-SB-13	0.81	—	—	—
^{18}F-FACT	1.94	0.28	Temporal occipital*	4
^{18}F-florbetapir	1.70	0.60	Putamen†	9
^{18}F-florbetaben	1.09	0.75	Global cortex*‡	45
^{18}F-flutemetamol	2.49	0.93	Posterior cingulate*	46
^{18}F-FDDNP	0.88	0.07	Global cortex§‖	33
^{18}F-AZD4694	3.26	1.26	Posterior cingulate*	36

*Estimated BP$_{ND}$ (DVR-1) from target V_T and cerebellar V_T in 2-tissue-compartment model.
†Estimated BP$_{ND}$ (DVR-1) from graphical plot (Zhou's method).
‡Frontal, lateral temporal, parietal, and posterior cingulate cortices.
§Estimated BP$_{ND}$ (simplified reference tissue model).
‖Orbital frontal, medial inferior frontal, anterior cingulate, superior temporal, parietal, medial inferior temporal, superior frontal, and entorhinal cortices and hippocampus.
Ref. = reference.

several possible reasons for this overestimation. One is the physiologic change in K_1 observed clinically in elderly subjects, especially those with AD. The other is the empiric scaling factor (3.43) introduced by Guo et al. (17), which compensates for the difference in K_1 between in vivo studies (pig) and mathematic modeling.

With regard to the outlier, of the 8 tracers in Table 3 only ^{18}F-FDDNP showed a higher clinical K_1 in the AD group (0.36) than in the healthy group (0.25). A good correlation between predicted and clinical K_1 in the healthy group was observed even when the ^{18}F-FDDNP K_1 data were included. We speculate that the reason ^{18}F-FDDNP behaved differently, especially in the case of AD, is the difference in its chemical structure from the other 7 tracers.

We also need to consider whether a given compound is a P-glycoprotein substrate. A substrate of P-glycoprotein allows active transportation of radioligand across the blood–brain barrier and thus does not fit well in Equation 2 (17). It has been reported that ^{11}C-PIB is not a substrate of P-glycoprotein (27,28); hence, ^{11}C-PIB can be assumed to be transported across the blood–brain barrier by passive diffusion. The amyloid radioligands we evaluated were shown not to be P-glycoprotein substrates, in that they were transported across the blood–brain barrier by passive diffusion as supported by the good correlation between predicted and clinical K_1 (Fig. 3A). However, when the method is applied to other candidate radioligands, the approach by which to determine whether a compound is a P-glycoprotein substrate will be an issue.

Predicted f_p, f_{ND}, and k_2

f_p and f_{ND} are parameters for the prediction of k_2 in Equation 4. For each radioligand, f_p and f_{ND} were predicted using the datasets shown in Figure 2. Even though there was inconsistent use of lipophilicity for estimation of f_p and f_{ND} between our study (which used Moriguchi log$P$) and the studies of Wan et al. (23) and Mauer et al. (24) (which used $c$log$P$), we observed positive correlations between predicted and clinical k_2 in the healthy and AD groups

(R^2 = 0.81 and 0.85, respectively) (Fig. 3B). This result supports the possibility that use of the Moriguchi log$P$ without in vitro experiments for f_p and f_{ND} estimation can be applied to other amyloid radioligands. There have been several studies with reported data sets for in silico log$P$, in vitro f_p, and f_{ND} for CNS drugs or radioligands (17,23,24,29). The data sets selected for use may change the predicted f_P and f_{ND}.

Predicted BP$_{ND}$ in Amyloid Imaging

B_{avail}, K_D, and f_{ND} are parameters for the prediction of BP$_{ND}$ in Equation 5. Among CNS radioligands, B_{avail} is not so varied
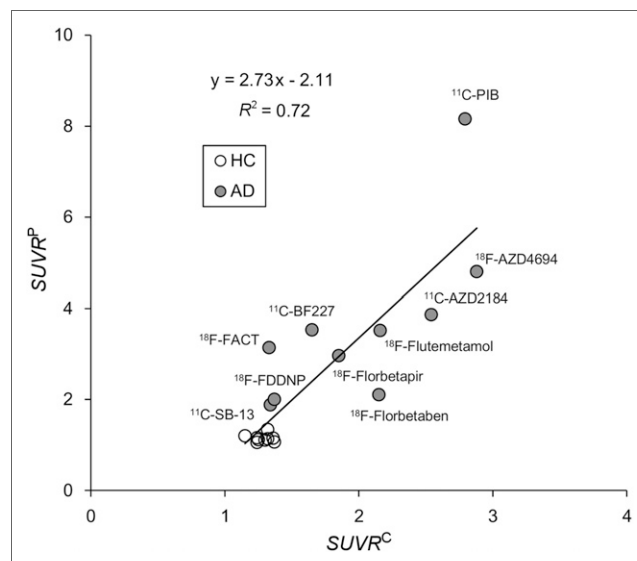

FIGURE 4. Comparison between predicted (y-axis) and clinical (x-axis) SUVR in healthy (HC) and AD subjects.

among subjects. However, in pathologic imaging such as amyloid PET, the Aβ burden in the brain is more than 10 times higher in AD patients than in healthy subjects. An appropriate B_{avail} is important in simulating progressive change in radioligand uptake. However, it is difficult to define an appropriate B_{avail} because of the regional and individual differences in the B_{avail} of Aβ plaques. It may be better to simulate a wide range of B_{avail} for the evaluation of radioligands in amyloid PET. Furthermore, the affinity of target radioligands for various types of Aβ plaque (diffuse, dense core, amorphous, and cerebrovascular amyloid) were not modeled in the current study. In vitro studies have demonstrated the different binding properties of each radioligand; for example, ^{11}C-BF-227 and ^{18}F-FACT preferentially bind to mature plaques (*4,5,30*). Previously reported differences in regional uptake between ^{18}F-FACT and ^{11}C-PIB may have been caused by differences in regional distribution between diffuse and dense-cored amyloid plaques (*31*). These binding properties concerning various kinds of Aβ plaque are difficult to simulate using biomathematic modeling and may be a current limitation of the method.

Using predicted f_{ND}, fixed B_{avail}, and in vitro K_D, predicted and clinical BP_{ND} correlated positively in the AD group ($R^2 = 0.63$) (Fig. 3C); however, this correlation was lower than that of K_1 and k_2. In the case of ^{11}C-PIB, predicted BP_{ND} was 5.44 and clinical BP_{ND} was 1.51 in the AD group (Table 4) (*2*). It can be speculated that this discrepancy results from differences between the B_{avail} used in our model and that observed in clinical studies or the effect of specific binding to tau in clinical studies (*32*).

Furthermore, in our study, in vitro K_D was obtained from published studies performed at different institutes and under different experimental conditions. We confirmed that an error in K_D propagates to BP_{ND} and to the final SUVR (Supplemental Fig. 1). If the present methodology were to be applied to within-institution screening using the same experimental protocol to measure K_D, the correlation between predicted and clinical BP_{ND} would improve.

Predicted Time–Activity Curves and SUVR

The proposed method has two major limitations when calculating time–activity curves: the use of a simplified model and the use of a common input function. In general, clinical time–activity curves in the target region of an amyloid PET study are expressed as a 2-tissue-compartment model, not a 1-tissue-compartment model (*2,4*). Therefore, the model used in our study—a simplified 1-tissue-compartment model involving only 3 kinetic parameters—may not be suitable for predicting time–activity curves in the target region. However, if a 2-tissue-compartment model were implemented for more accurate modeling, a larger number of microparameters (e.g., K_1, k_2, k_3, and k_4) would be necessary, and k_4 would be too small to be predicted accurately. Therefore, we used the simplified 1-tissue-compartment model while reducing the number of parameters relative to the 2-tissue-compartment model. Furthermore, it is ideal to use the measured time-course of the radioactivity concentration in human plasma for each radioligand. We found that there were only small visual differences in plasma input functions among several studies (*4,7,33–36*). Therefore, we decided to use a common arterial input function of ^{11}C-BF227 (Fig. 1B). Further studies will be required to investigate how the error caused by the input function influences the outcome.

Despite its limitations, the method simulated a tendency toward faster clearance of ^{18}F-FACT than of ^{11}C-BF227 (Supplemental Fig. 2), similar to the observations of a clinical study (*4*). However, in the case of ^{11}C-PIB, we observed a difference in the shape of the target region between the clinical (*2*) and predicted time–activity curves (Supplemental Fig. 2). The method may require further modification to generate more realistic time–activity curves. Overall, the predicted and clinical SUVRs correlated well (Fig. 4), even though there was a discrepancy in the SUVRs for ^{11}C-PIB.

Application to Candidate Compounds

The method may be used to support screening of candidate compounds before in vivo PET studies begin. There are unmodeled factors, such as pathologic changes in K_1 due to aging and disease, the effect of spill-in from nonspecific binding in white matter to the cortical regions, the possible presence of P-glycoprotein substrate, and differences in binding properties among various types of Aβ plaque. Consideration of these factors may improve accuracy, but compounding errors due to having too many factors may lead to greater complications and variations. We believe the current model considers those factors that are important in ensuring reliable prediction of the SUVRs of amyloid PET radioligands. However, to evaluate the clinical applicability of candidate compounds, we need to achieve not only a large difference in SUVRs between healthy and AD groups but also the statistical power to classify the two groups. We plan to undertake such an evaluation.

CONCLUSION

The SUVRs that the proposed biomathematic model predicted for 10 amyloid tracers correlated well with the clinical SUVRs obtained from in vivo studies. The model showed good reliability and, hence, the potential to be applied to other amyloid radioligands.

DISCLOSURE

REFERENCES

1. Klunk WE, Lopresti BJ, Ikonomovic MD, et al. Binding of the positron emission tomography tracer Pittsburgh compound-B reflects the amount of amyloid-β in Alzheimer's disease brain but not in transgenic mouse brain. *J Neurosci.* 2005;25:10598–10606.

2. Price JC, Klunk WE, Lopresti BJ, et al. Kinetic modeling of amyloid binding in humans using PET imaging and Pittsburgh compound-B. *J Cereb Blood Flow Metab.* 2005;25:1528–1547.

3. Waragai M, Okamura N, Furukawa K, et al. Comparison study of amyloid PET and voxel-based morphometry analysis in mild cognitive impairment and Alzheimer's disease. *J Neurol Sci.* 2009;285:100–108.

4. Shidahara M, Watabe H, Tashiro M, et al. Quantitative kinetic analysis of PET amyloid imaging agents [11C]BF227 and [18F]FACT in human brain. *Nucl Med Biol.* 2015;42:734–744.

5. Kudo Y, Okamura N, Furumoto S, et al. 2-(2-[2-dimethylaminothiazol-5-yl] ethenyl)-6- (2-[fluoro]ethoxy)benzoxazole: a novel PET agent for in vivo detection of dense amyloid plaques in Alzheimer's disease patients. *J Nucl Med.* 2007;48:553–561.

6. Furukawa K, Okamura N, Tashiro M, et al. Amyloid PET in mild cognitive impairment and Alzheimer's disease with BF-227: comparison to FDG-PET. *J Neurol.* 2010;257:721–727.

7. Ito H, Shimada H, Shinotoh H, et al. Quantitative analysis of amyloid deposition in Alzheimer disease using PET and the radiotracer ^{11}C-AZD2184. *J Nucl Med.* 2014;55:932–938.

8. Verhoeff NP, Wilson AA, Takeshita S, et al. In-vivo imaging of Alzheimer disease β-amyloid with [11C]SB-13 PET. *Am J Geriatr Psychiatry.* 2004;12:584–595.

9. Wong DF, Rosenberg PB, Zhou Y, et al. In vivo imaging of amyloid deposition in Alzheimer disease using the radioligand ^{18}F-AV-45 (florbetapir [corrected] F 18). *J Nucl Med.* 2010;51:913–920.

10. Camus V, Payoux P, Barre L, et al. Using PET with ^{18}F-AV-45 (florbetapir) to quantify brain amyloid load in a clinical environment. *Eur J Nucl Med Mol Imaging.* 2012;39:621–631.

11. Rowe CC, Ackerman U, Browne W, et al. Imaging of amyloid β in Alzheimer's disease with ^{18}F-BAY94-9172, a novel PET tracer: proof of mechanism. *Lancet Neurol.* 2008;7:129–135.

12. Thurfjell L, Lotjonen J, Lundqvist R, et al. Combination of biomarkers: PET [^{18}F]flutemetamol imaging and structural MRI in dementia and mild cognitive impairment. *Neurodegener Dis.* 2012;10:246–249.

13. Hatashita S, Yamasaki H, Suzuki Y, Tanaka K, Wakebe D, Hayakawa H. [^{18}F] flutemetamol amyloid-beta PET imaging compared with [^{11}C]PIB across the spectrum of Alzheimer's disease. *Eur J Nucl Med Mol Imaging.* 2014;41:290–300.

14. Tauber C, Beaufils E, Hommet C, et al. Brain [^{18}F]FDDNP binding and glucose metabolism in advanced elderly healthy subjects and Alzheimer's disease patients. *J Alzheimers Dis.* 2013;36:311–320.

15. Rowe CC, Pejoska S, Mulligan RS, et al. Head-to-head comparison of ^{11}C-PiB and ^{18}F-AZD4694 (NAV4694) for β-amyloid imaging in aging and dementia. *J Nucl Med.* 2013;54:880–886.

16. Innis RB, Cunningham VJ, Delforge J, et al. Consensus nomenclature for in vivo imaging of reversibly binding radioligands. *J Cereb Blood Flow Metab.* 2007;27: 1533–1539.

17. Guo Q, Brady M, Gunn RN. A biomathematical modeling approach to central nervous system radioligand discovery and development. *J Nucl Med.* 2009;50: 1715–1723.

18. Brockschnieder D, Schmitt-Willich H, Heinrich T, et al. Preclinical characterization of a novel class of ^{18}F-labeled PET tracers for amyloid-β. *J Nucl Med.* 2012;53:1794–1801.

19. van de Waterbeemd H, Camenisch G, Folkers G, Chretien JR, Raevsky OA. Estimation of blood-brain barrier crossing of drugs using molecular size and shape, and H-bonding descriptors. *J Drug Target.* 1998;6:151–165.

20. Laruelle M, Slifstein M, Huang Y. Relationships between radiotracer properties and image quality in molecular imaging of the brain with positron emission tomography. *Mol Imaging Biol.* 2003;5:363–375.

21. Guo Q, Owen DR, Rabiner EA, Turkheimer FE, Gunn RN. Identifying improved TSPO PET imaging probes through biomathematics: the impact of multiple TSPO binding sites in vivo. *Neuroimage.* 2012;60:902–910.

22. Moriguchi I, Hirono S, Liu Q, Nakagome I, Matsushita Y. Simple method of calculating octanol/water partition coefficient. *Chem Pharm Bull (Tokyo).* 1992;40: 127–130.

23. Wan H, Rehngren M, Giordanetto F, Bergstrom F, Tunek A. High-throughput screening of drug-brain tissue binding and in silico prediction for assessment of central nervous system drug delivery. *J Med Chem.* 2007;50:4606–4615.

24. Maurer TS, Debartolo DB, Tess DA, Scott DO. Relationship between exposure and nonspecific binding of thirty-three central nervous system drugs in mice. *Drug Metab Dispos.* 2005;33:175–181.

25. Villemagne VL, Klunk WE, Mathis CA, et al. Aβ imaging: feasible, pertinent, and vital to progress in Alzheimer's disease. *Eur J Nucl Med Mol Imaging.* 2012;39:209–219.

26. Steinerman JR, Irizarry M, Scarmeas N, et al. Distinct pools of Aβ in Alzheimer's disease brain: a clinical-pathological study. *Arch Neurol.* 2008;65: 906–912.

27. Tournier N, Valette H, Peyronneau MA, et al. Transport of selected PET radiotracers by human P-glycoprotein (ABCB1) and breast cancer resistance protein (ABCG2): an in vitro screening. *J Nucl Med.* 2011;52:415–423.

28. Ishiwata K, Kawamura K, Yanai K, Hendrikse NH. In vivo evaluation of P-glycoprotein modulation of 8 PET radioligands used clinically. *J Nucl Med.* 2007;48:81–87.

29. Summerfield SG, Read K, Begley DJ, et al. Central nervous system drug disposition: the relationship between in situ brain permeability and brain free fraction. *J Pharmacol Exp Ther.* 2007;322:205–213.

30. Furumoto S, Okamura N, Furukawa K, et al. A ^{18}F-labeled BF-227 derivative as a potential radioligand for imaging dense amyloid plaques by positron emission tomography. *Mol Imaging Biol.* 2013;15:497–506.

31. Ito H, Shinotoh H, Shimada H, et al. Imaging of amyloid deposition in human brain using positron emission tomography and [^{18}F]FACT: comparison with [^{11}C]PIB. *Eur J Nucl Med Mol Imaging.* 2014;41:745–754.

32. Harada R, Okamura N, Furumoto S, et al. Comparison of the binding characteristics of [^{18}F]THK-523 and other amyloid imaging tracers to Alzheimer's disease pathology. *Eur J Nucl Med Mol Imaging.* 2013;40:125–132.

33. Yaqub M, Boellaard R, van Berckel BN, et al. Evaluation of tracer kinetic models for analysis of [^{18}F]FDDNP studies. *Mol Imaging Biol.* 2009;11:322–333.

34. Heurling K, Buckley C, Van Laere K, Vandenberghe R, Lubberink M. Parametric imaging and quantitative analysis of the PET amyloid ligand [^{18}F]flutemetamol. *Neuroimage.* 2015;121:184–192.

35. Edison P, Brooks DJ, Turkheimer FE, Archer HA, Hinz R. Strategies for the generation of parametric images of [^{11}C]PIB with plasma input functions considering discriminations and reproducibility. *Neuroimage.* 2009;48:329–338.

36. Cselényi Z, Jonhagen ME, Forsberg A, et al. Clinical validation of ^{18}F-AZD4694, an amyloid-β-specific PET radioligand. *J Nucl Med.* 2012;53:415–424.

37. Mathis CA, Wang Y, Holt DP, Huang GF, Debnath ML, Klunk WE. Synthesis and evaluation of ^{11}C-labeled 6-substituted 2-arylbenzothiazoles as amyloid imaging agents. *J Med Chem.* 2003;46:2740–2754.

38. Johnson AE, Jeppsson F, Sandell J, et al. AZD2184: a radioligand for sensitive detection of β-amyloid deposits. *J Neurochem.* 2009;108:1177–1186.

39. Ikonomovic MD, Klunk WE, Abrahamson EE, et al. Post-mortem correlates of in vivo PiB-PET amyloid imaging in a typical case of Alzheimer's disease. *Brain.* 2008;131:1630–1645.

40. Choi SR, Golding G, Zhuang Z, et al. Preclinical properties of ^{18}F-AV-45: a PET agent for Aβ plaques in the brain. *J Nucl Med.* 2009;50:1887–1894.

41. Zhang W, Oya S, Kung MP, Hou C, Maier DL, Kung HF. F-18 polyethylene-glycol stilbenes as PET imaging agents targeting Aβ aggregates in the brain. *Nucl Med Biol.* 2005;32:799–809.

42. Juréus A, Swahn BM, Sandell J, et al. Characterization of AZD4694, a novel fluorinated Aβ plaque neuroimaging PET radioligand. *J Neurochem.* 2010;114: 784–794.

43. Agdeppa ED, Kepe V, Liu J, et al. Binding characteristics of radiofluorinated 6-dialkylamino-2-naphthylethylidene derivatives as positron emission tomography imaging probes for β-amyloid plaques in Alzheimer's disease. *J Neurosci.* 2001;21:RC189.

44. McNamee RL, Yee SH, Price JC, et al. Consideration of optimal time window for Pittsburgh compound B PET summed uptake measurements. *J Nucl Med.* 2009;50: 348–355.

45. Becker GA, Ichise M, Barthel H, et al. PET quantification of ^{18}F-florbetaben binding to β-amyloid deposits in human brains. *J Nucl Med.* 2013;54:723–731.

46. Nelissen N, Van Laere K, Thurfjell L, et al. Phase 1 study of the Pittsburgh compound B derivative ^{18}F-flutemetamol in healthy volunteers and patients with probable Alzheimer disease. *J Nucl Med.* 2009;50:1251–1259.